Received: 7 September 2020 | Revised: 23 October 2020 | Accepted: 26 October 2020

DOI: 10.1111/ahe.12632

ORIGINAL ARTICLE

ANATOMIA HISTOLOGIA EMBRYOLOGIA JOURNAL OF VETERINARY MEDICINE | WILEY

Micro-anatomy of the ear of the southern white rhinoceros (*Ceratotherium simum simum*)

Mickaël P. Robert[1] | Ann Carstens[1] | Frederik C. de Beer[2] | Jakobus W. Hoffman[2] | Gerhard Steenkamp[1]

[1]Faculty of Veterinary Science, Department of Companion Animal Clinical Studies, University of Pretoria, Onderstepoort, South Africa

[2]Micro-Focus X-ray Tomography Facility (MIXRAD), South African Nuclear Energy Corporation SOC Ltd. (Necsa), Pelindaba, South Africa

Correspondence
Mickaël P. Robert, Centre Hospitalier Vétérinaire Equin de Livet, 1497 Route de Castillon, 14140 Livarot Pays d'Auge, France.
Email: dr.mickael.robert@gmail.com

Funding information
DST-NRF, Grant/Award Number: UID72310

Abstract

The white rhinoceros is the largest of the five extant rhinoceros species. The population is declining rapidly because of intense poaching. However, normal anatomical descriptions in this species are lacking. The purpose of this study is to describe the osseous anatomy of the middle and inner ear of the southern white rhinoceros using micro-focus X-ray computed tomography imaging. Four temporal bones obtained from two 1-day old southern white rhinoceros preserved in 10% formalin were scanned. Tri-dimensional reconstructions were obtained and volumes of the middle ear ossicles and inner ear structures were calculated. Excellent high spatial resolution 3D images were obtained for all samples and virtual models of the auditory ossicles and bony labyrinth were generated. Visualization of the tympanic membrane, middle ear and inner ear structures was possible in all samples. Whereas the *stapes* and *incus* had a shape similar to their human or equine counterparts, the *malleus* showed a unique appearance with a long rostral branch projecting latero-distally to the *manubrium*. The cochlea described 2 turns rostro-laterally around its axis, with a medial direction of rotation. However, identification of the soft tissue structures of the middle ear was sometimes difficult and visualization of the small structures of the membranous labyrinth was not possible using this formalin fixation and alternative techniques should be investigated. Further investigations are needed in order to provide a complete virtual model including both soft and bone tissues of this difficultly accessible region.

KEYWORDS

inner ear, micro-focus X-ray CT, middle ear, southern white rhinoceros, tympanic membrane

1 | INTRODUCTION

The white rhinoceros, also called square-lipped rhinoceros or grass rhinoceros, is the largest of the five extant rhinoceros species and one of the two African species (Owen-Smith, 2013). Whereas two subspecies are officially recognized, the southern white rhinoceros *Ceratotherium simum simum* and the northern white rhinoceros *Ceratotherium simum cottoni*, the latter is considered nearly extinct after the last male died in March 2018, leaving only two females in Kenya (Anonymous, 2018; Lemonde.fr, 2018). Today, the southern white rhinoceros is classified as Near Threatened because of intense poaching (Emslie, 2012; Knight, 2017; Robin des Bois, 2018; TRAFFIC, 2018). The most recent estimates for this species are only 20,000 animals remaining in Africa (Knight, 2017).

The data that support the findings of this study are available from the corresponding author upon reasonable request.

Recently, it was stated that normal anatomical descriptions in the rhinoceros were lacking (Galateanu et al., 2013). Studies have been published looking at the radiographic anatomy of the hind feet (Dudley et al., 2015), computed tomography (CT) anatomy of the head and paranasal sinuses of the white rhinoceros (Fritsch et al., 2004; Gerard et al., 2018; WitmerLab, 2012). Nevertheless, none of those studies investigated the middle and inner ear of the white rhinoceros.

The ear or vestibulocochlear organ is a sensory organ located in the temporal bone and intended for the perception of sounds but also changes of position of the body and more particularly of the head. It consists of an external -, middle - and inner ear (Collin, 2006).

Whereas it has been extensively described in the domestic mammals (Baljit, 2017; Barone, 2010, 2011), only ancient and rare reports describe the gross anatomy of the ear of the rhinoceros (Owen, 1866; Vicq-D'Azyr & Cloquet, 1819). When focusing on the middle and inner ear, Owen (1866) first presented a short description of the rhinoceros's ossicles chain, soon followed by Doran (1876). Hyrtl (1873) described the inner ear of the extinct woolly rhinoceros (*Coelodonta antiquitatis*). However, to our knowledge, none of those studies looked at the southern white rhinoceros.

Schellhorn (2018) evaluated the inner ear of the extant rhinoceroses using micro-focus X-ray computed tomography (μXCT) studies. He concluded that the position of the lateral semicircular canal (LSC) provides information to interpret usual head postures linked to feeding preferences. In particular, the white rhinoceros, a strict grazer, had the most downward oriented head posture when LSC placed horizontally. But no particular anatomical description of the inner ear was given.

In human anatomical sciences, μXCT imaging has been shown to provide high-resolution three dimensional (3D) morphological and anatomical data in the middle and inner ear regions in a non-destructive manner (Glueckert et al., 2018; Lee et al., 2010; van den Boogert et al., 2018). Doing so, it also yielded greater understanding of the relevant middle and inner ear functional anatomy and permitted to create virtual temporal bone surgical simulators (Wiet et al., 2005). It is also anticipated that μXCT imaging will help designing new surgical approaches, ossicular reconstructive materials and will contribute in improving and developing new cochlear and vestibular implants (Glueckert et al., 2018; Green et al., 1990; Mason et al., 2000; Qiu et al., 2003; van den Boogert et al., 2018).

The purpose of this study is to describe in detail the osseous anatomy of the middle and inner ear of the southern white rhinoceros *Ceratotherium simum simum* using μXCT imaging.

2 | MATERIALS AND METHODS

Two 1-day old southern white rhinoceros heads were donated to us for research purpose by a rhinoceros breeding farm. One of the rhinoceros calves drowned (case 1) and the other was trampled to death (case 2).

For this study, the heads were preserved in 10% formalin and transected sagittally and then transversely rostral to the ear region using a band saw.

Consequently, the four samples (left and right temporal bones of cases 1 and 2) were scanned using a micro-focus X-ray CT unit (Nikon XTH 225 ST, Nikon Metrology, France) at the Micro-Focus X-ray Tomography Facility (MIXRAD) of the South African Nuclear Energy Corporation SOC Ltd (Necsa) using 100 kV and 100 μA as parameters and focusing on the middle and inner ear region (Hoffman & de Beer, 2012).

The obtained stack images emanating from the 3D reconstruction process were analysed using VGStudio Max version 3.2 3D analytical software (Volume Graphics, Germany) and saved in TIFF format for further evaluation. Tri-dimensional reconstructions were obtained and volumes of the middle ear ossicles and inner ear structures (semicircular canals, vestibule and cochlea) were calculated using the same software.

Approval has been obtained from the Animal Ethics Committee of the University of Pretoria (Project V088-18). Additionally, permission has been obtained to do research in terms of section 20 of the animal diseases act, 1984 (ACT NO.35 of 1984).

3 | RESULTS

Excellent high spatial resolution 3D images were obtained for all samples, with a mean voxel size of $(39.5 \times 39.5 \times 39.5) \pm 6.4\ \mu m^3$ (Table 1). Scanning time was 66.8 min for each sample.

Excellent contrast between the temporal bone and peripheral air and fluids due to their different densities was achieved in order to

TABLE 1 Voxel size, inner ear volume and middle ear ossicles volume measured using micro-focus X-ray computed tomography images in the left and right ear of two southern white rhinoceroses

	Rhino 1		Rhino 2		
	Left ear	Right Ear	Left ear	Right Ear	Mean (*SD*)
Voxel size (μm^3)	34.1	35.8	39.8	48.4	39.5 (6.4)
Inner ear volume (mm^3)	240.65	189.71	234.88	232.4	224.41 (23.39)
Middle ear ossicles volume (mm^3)	28.82	31.41	34.11	37.55	32.97 (3.74)

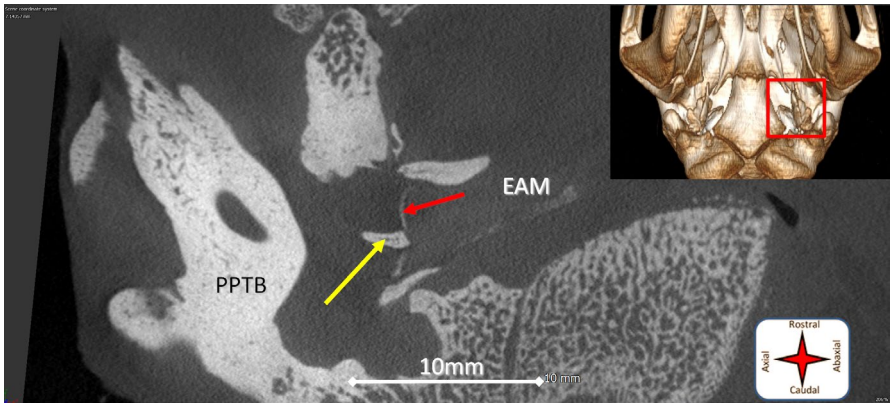

FIGURE 1 Micro-focus X-ray computed tomography 2D slice image obtained from the left ear of case 1, coronal plane. The red arrow shows the tympanic membrane. The yellow arrow highlights the handle of the hammer (*manubriummalleus*) attached to the tympanic membrane. PPTB: Petrous part of the temporal bone. EAM: External acoustic meatus. Scale is 10 mm. The top right insert shows the region that has been scanned with the μXCT; this ventral view of case 1 was obtained with a 128 slice CT scan

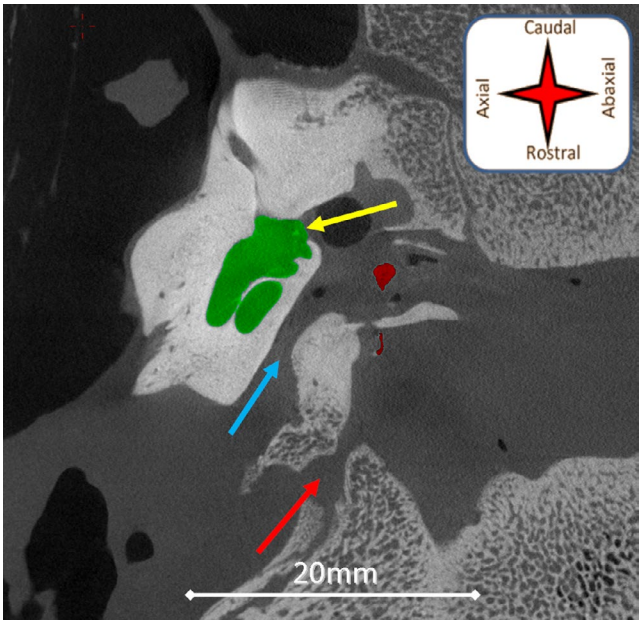

FIGURE 2 Micro-focus X-ray computed tomography 2D slice image obtained from the right ear of case 2, coronal plane. The green area shows the cochlea. The red areas highlight the handle and the rostral branch of the hammer (*malleus*). The blue arrow indicates the auditory tube. The red arrow indicates the path of the internal carotid artery. The yellow arrow shows the round window (*fenestra cochleae*). Scale is 20 mm

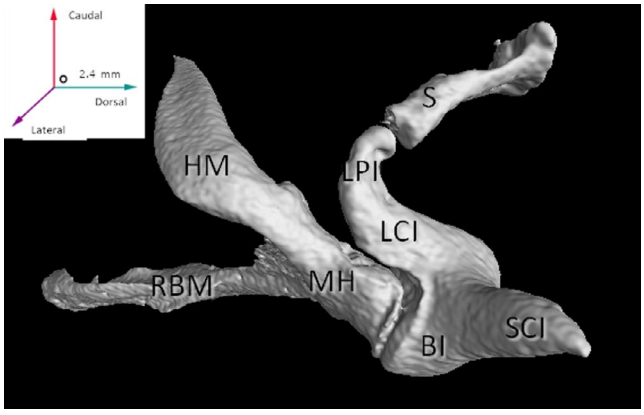

FIGURE 3 3D volume reconstruction of the auditory ossicles obtained from the left ear of case 1. The body of the*incus*(BI), short crus of the*incus*(SCI), long crus of the*incus*(LCI), lenticular process of the*incus*(LPI),*malleus*head (MH), handle of the*malleus*(HM), rostral branch of the*malleus*(RBM) and*stapes*(S) are all visible

visualize the tympanic membrane, middle ear and inner ear structures inside the heads (Figures 1 and 2).

Volumes of the middle ear ossicles and inner ear structures (semicircular canals, vestibule and cochlea) are reported in Table 1.

Tri-dimensional reconstructions of the middle ear ossicles and inner ear structures were of high quality.

The hammer (*malleus*) has a Y-shaped configuration. The rostral branch of the Y appears straight, lateral ventrally, longer than the handle of the hammer, facing rostral. The handle of the hammer lies more sagittally ventrally, is curved (ventro-medial to dorso-lateral), points down and attaches to the tympanic membrane. The base of the Y-shaped *malleus* is the head of the hammer. It is dorsal to the handle and the rostral branch and articulates caudally with the body of the *incus* through the incudomalleolar joint which is clearly visible in the 2D slice (Figure 1 and Video S1) and 3D volumes (Figures 3 and 4).

The *incus* has more of a ladle shape. The cup of the ladle is the body of the *incus*, is wider and articulates with the head of the *malleus* rostrally. The handle of the ladle, or long crus (or process) of the *incus*, then curves caudo-medially, forming the lenticular process of the *incus*, articulating with the head of the stirrup (*stapes*) through the incudostapedial joint. Dorsally the cup part of the ladle (body of the *incus*) sends a lateral pointy projection, the short crus of the *incus* (Figures 3 and 5).

The *stapes* is clearly visible, smaller than the other two ossicles. Its head articulates with the long process of the *incus*, whereas its base or footplate is attached to the membrane, or annular ligament, of the oval window (*fenestra ovalis*) on the vestibule (Figures 3, 5 and

6). Because of the fixative fluid contained in the middle ear, no soft tissue structures could be identified.

When looking at the bony structures of the inner ear, or osseous labyrinth, the cochlea appears as a spiral channel starting at the vestibule and describing 2 turns rostro-laterally around its axis, with an medial direction of rotation (Figures 2, 7–9;). The tympanic and vestibular ducts with associated septa (the osseous spiral lamina) are visible in the cochlea, as well as the central *modiolus*. The cochlear aqueduct is also visible running from the basal cochlear turn to the *posterior cranial fossa* (Figure 8). Similarly, the vestibular aqueduct between the vestibule and the *posterior cranial fossa* is also observed.

All 3 semicircular canals emerge from the caudo-dorsal part of the vestibule (Figures 7, 10–12). The anterior and the posterior canals have a common part, or common crus, medially, whereas the lateral one is clearly isolated. The *ampullae* of the canals, one anterior, one posterior and one lateral are also visible.

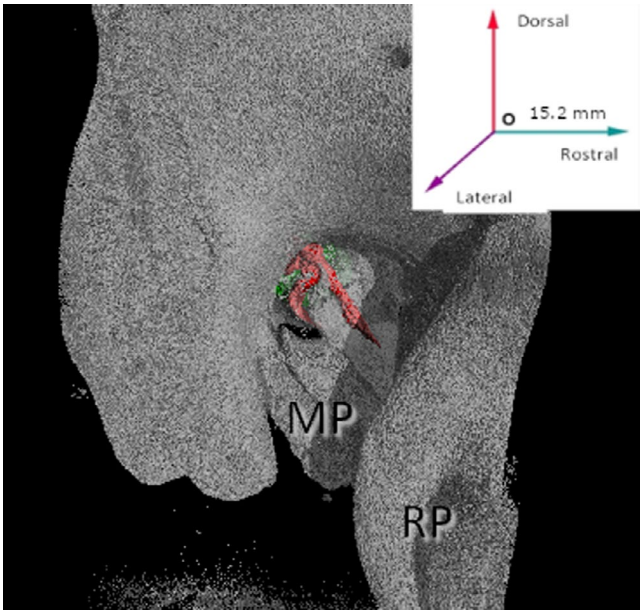

FIGURE 4 3D volume reconstruction of the external acoustic meatus with auditory ossicles (red) and inner ear (green) in place, obtained from the left ear of case 2. Lateral view. The two branches of the*malleus*are clearly visible. MP: Mastoid process of the temporal bone; RP: Retroarticular process (according to Endo et al., 1998)

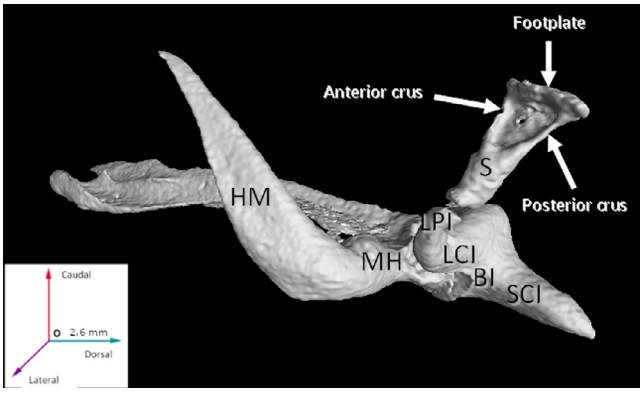

FIGURE 5 3D volume reconstruction of the auditory ossicles obtained from the left ear of case 1. The body of the*incus*(BI), short crus of the*incus*(SCI), long crus of the*incus*(LCI), lenticular process of the*incus*(LPI),*malleus*head (MH), handle of the*malleus*(HM) and*stapes*(S) with his anterior and posterior crus, as well as footplate, are all visible

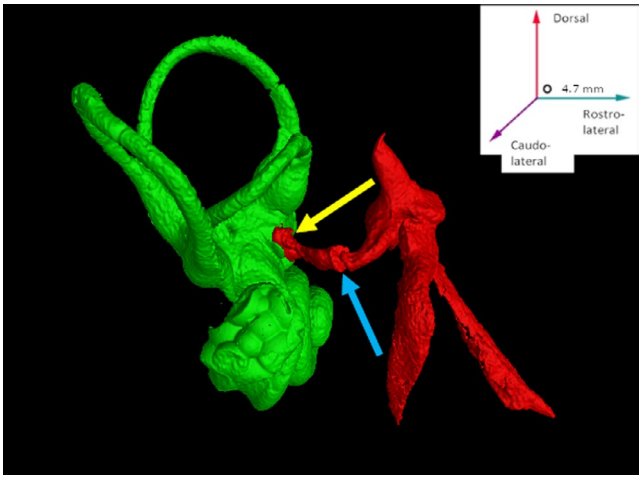

FIGURE 6 3D volume reconstruction of the auditory ossicles (red) and osseous labyrinth (green) obtained from the left ear of case 2. Lateral view. The attachment of the base of the*stapes*to the*fenestra ovalis*(yellow arrow) as well as the incudostapedial joint (blue arrow) are clearly visible

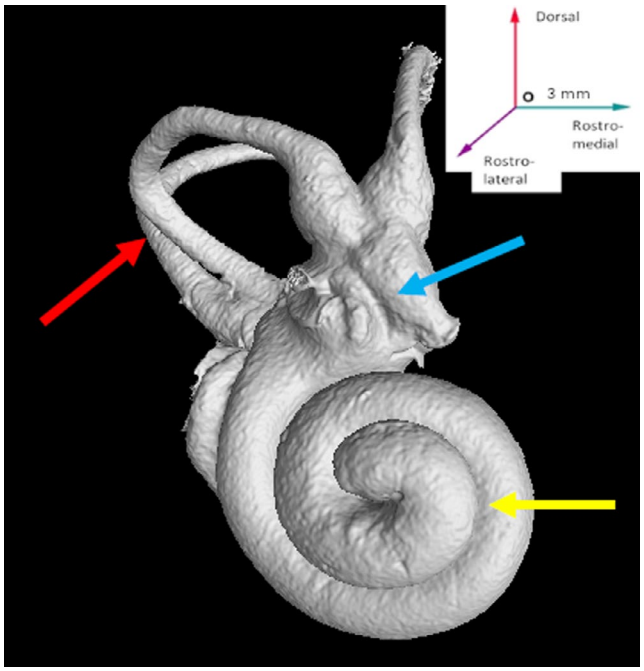

FIGURE 7 3D volume reconstruction of the bony structures of the inner ear, obtained from the left ear of case 1. Rostro-lateral view. The yellow arrow highlights the 2 turns of the spiral cochlea. The blue arrow points to the vestibule. The red arrow points to the semicircular canals

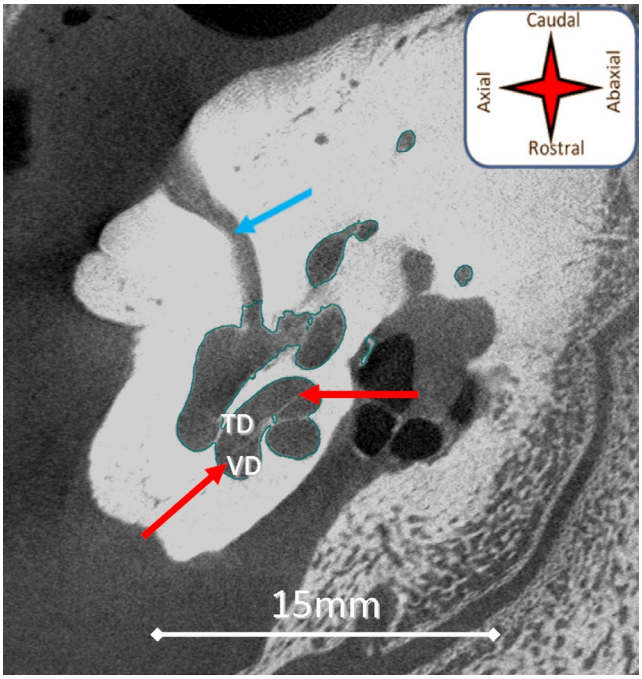

FIGURE 8 Micro-focus X-ray computed tomography 2D slice image obtained from the left ear of case 2, coronal plane. The tympanic (TD) and vestibular (VD) ducts with associated osseous spiral lamina (red arrows) are visible in the cochlea. The cochlear aqueduct is also clearly visible (blue arrow)

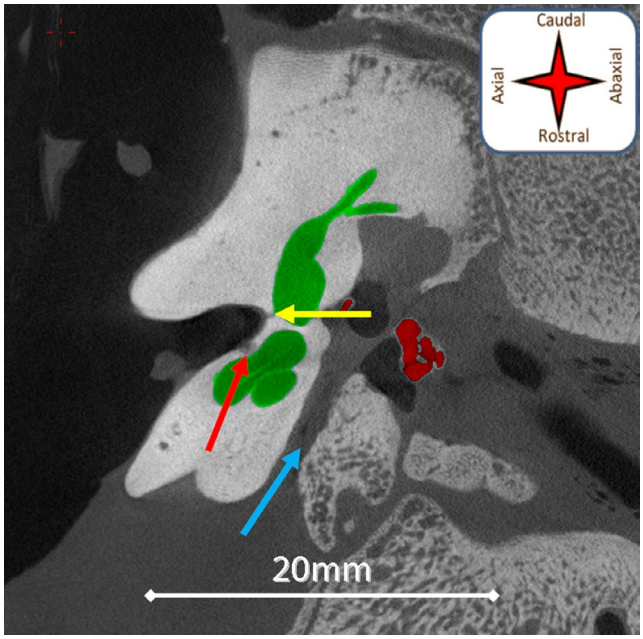

FIGURE 9 Micro-focus X-ray computed tomography 2D slice image obtained from the right ear of case 2, coronal plane. The green area shows the cochlea. The red areas highlight the*stapes*and the incudomalleolar joint. The facial canal (blue arrow) and tracts of the cochlear (red arrow) and vestibular (yellow arrow) nerves are visible. IAM: Internal acoustic meatus

In the vestibule, even though some septa are sometimes visible, it is not possible to visualize the utricle and saccule.

Similar to human anatomical studies, the position of the nerves (facial and vestibulocochlear) and vessels (internal carotid artery, sigmoid sinus and internal jugular vein) associated to the middle and inner ears could also be assumed (Figures 2 and 12) (Moon & Lee, 2014; Nayak, 2001; Qiu et al., 2003).

4 | DISCUSSION

Micro-focus X-ray computed tomography imaging allowed us to acquire excellent 3D virtual digital images of the tympanic membrane, middle ear and inner ear structures on all our samples. We were able to describe the relevant micro-anatomy of these structures in the southern white rhinoceros and to create virtual models of the auditory ossicles and bony labyrinth.

The mean image resolution in the present study was 39.5 μm^3 per voxel. This is similar to previous reports modelling the human middle ear where voxel sizes ranging from 19.5 to 76.0 μm^3 were used (Lee et al., 2010; Wang et al., 2007). However, the most recent studies investigating the human inner ear now use much higher resolutions, between 5.5 and 15 μm per voxel (Glueckert et al., 2018; van den Boogert et al., 2018). One of the main limitations of using such high-resolutions is the comparatively long exposure and hence scanning time per specimen. The scanning time with our parameters was just above an hour. The only previous study using μXCT on the ear in the rhinoceros had a higher voxel size of 126–309 μm and did not describe the actual anatomy of the region (Schellhorn, 2018).

The μXCT scanning parameters used were 100 kV and 100 μA. This is comparable to previous reports where values between 40–70 kV and 114–200 μA were used in human samples (Glueckert et al., 2018; Wiet et al., 2005). The higher scanning energy (kV) can be due to the superior size of our rhinoceros samples and the need to achieve good penetration of X-rays.

The scanned temporal bone specimens were fixed in formalin. This technique has been previously used in human studies (Wiet et al., 2005). It prevents movement that could occur with frozen samples melting during image acquisition. However, identification of soft tissue structures was sometimes difficult due to their similar densities. Alternative techniques to formalin-fixed μXCT imaging are possible in order to better describe the soft tissue structures of the middle and inner ear of the southern white rhinoceros. For example, 3D virtual models of the human ear were previously obtained from scanned histological sections, allowing visualization of muscles, nerves and vessels (Green et al., 1990; Sorensen et al., 2002; Wang et al., 2007). Yet, this technique can display compression artefacts and imperfect alignment. Another option would be to add high-field Magnetic Resonance Imaging (MRI) images to our μXCT images to include soft tissue structures in our model (Wiet et al., 2002, 2005). Finally, recent reports showed the benefits of fixing temporal bones with osmium tetroxide solution (OsO_4) as a contrast enhancer and decalcifying them with Ethylenediaminetetraacetic Acid (EDTA). This process gives extreme detail of the membranous labyrinth and

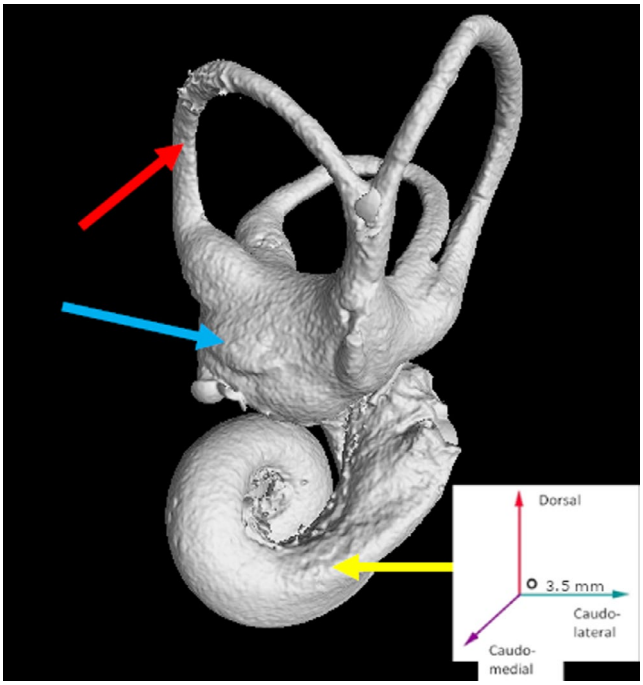

FIGURE 10 3D volume reconstruction of the bony structures of the inner ear, obtained from the left ear of case 1. Caudo-medial view. The yellow arrow highlights the 2 turns of the spiral cochlea. The blue arrow points to the vestibule. The red arrow points to the semicircular canals

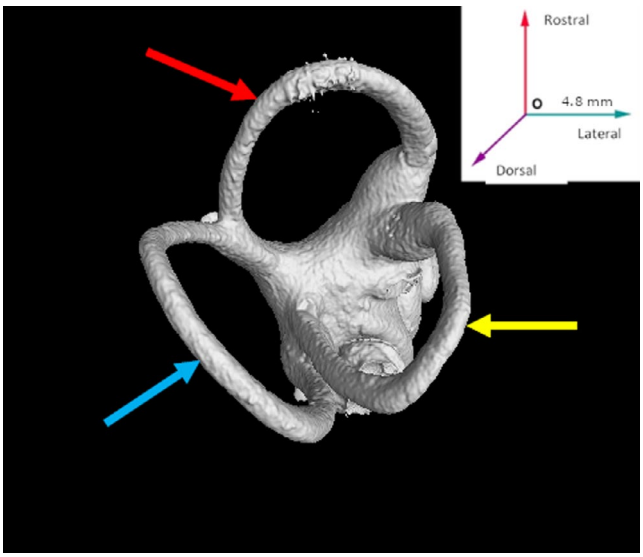

FIGURE 11 3D volume reconstruction of the bony structures of the inner ear, obtained from the left ear of case 1. Dorsal view. The yellow arrow highlights the lateral semicircular canal. The blue arrow points to the posterior semicircular canal. The red arrow points to the anterior semicircular canal

neural structures of the human inner ear, permitting observation of individual neurons and of the organ of Corti (Glueckert et al., 2018; van den Boogert et al., 2018).

The auditory ossicles were visible on all samples and 3D models we generated. Whereas the *stapes* and *incus* had a shape similar to

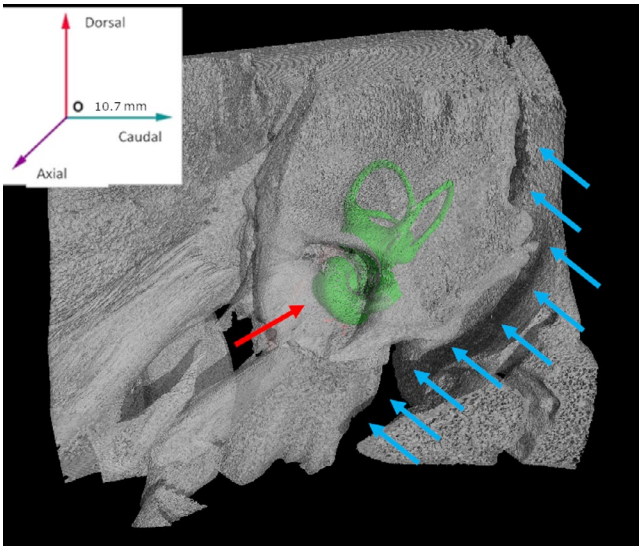

FIGURE 12 3D volume reconstruction of the inner ear (green) obtained from the left ear of case 1. Medial view. The orientation of the cochlea and semicircular canals relative to the internal acoustic meatus (red arrow) through which runs the vestibulocochlear and facial nerves is shown. The tract of the sigmoid sinus and internal jugular vein is highlighted by the blue arrows (according to Qiu et al., 2003)

their human or equine counterparts, the *malleus* showed a unique appearance with a long rostral branch projecting latero-distally to the *manubrium*. This is probably what Owen (1866) described as a bifid head of the *malleus*. This rostral branch could represent an overdeveloped form of the muscular process observed in ruminants, where the tensor tympani muscle normally inserts (Botti et al., 2006). Alternatively, this rostral branch is more likely to be the *processus gracilis* and associated bony lamella, as described by Doran (1876). Further details about this rostral branch and its potential function could be obtained using micro-dissection. In addition, no particular muscle process, as observed in cattle, was observed on the *stapes* for the stapedius muscle.

It has previously been stated that the most obvious variation in the inner ear of mammals comes with the number of turns of the cochlear coil (Webster, 1966). Whereas 2.5–2.75 turns have been described in the human cochlea (Curtin et al., 2011; Green et al., 1990) and 3 turns in the equine one (Collin, 2006), only two turns were detected within the 3D micro-X-ray CT volumes of the cochlea of the southern white rhinoceros.

Distinguishing the perilymphatic spaces from the endolymphatic space and visualization of the small structures of the membranous labyrinth was not possible on our images. This could be investigated in future studies using special fixatives or higher scanning resolutions (van den Boogert et al., 2018).

The orientation of the semicircular canals in the southern white rhinoceros seems similar to what has been described in men and horses (Collin, 2006; Green et al., 1990).

Looking at the volume of the inner ear, it is interesting to note that southern white rhinoceros neonates have values very similar

to humans. Indeed, we report a volume of 224.41 mm^3 which is comparable to 192.5–227.8 mm^3 reported in people (Buckingham & Valvassori, 2001; Melhem et al., 1998). However, none of those studies used high-resolution µXCT images, which makes an accurate comparison difficult to perform. Additionally, whereas no age- or sex-related differences in the inner ear volumetric measurements were found in people (Melhem et al., 1998), such information is currently missing in the southern white rhinoceros. The apparently small volume of the inner ear of the rhinoceros despite its important size could partially be explained by its shorter cochlea.

The paths of the nerves (mainly facial) and vessels (internal carotid artery and jugular bulb) were somewhat detectable using human descriptions, but yet appeared difficult with some variations from what has been described in men (Moon & Lee, 2014; Nayak, 2001; Qiu et al., 2003). Once again, additional imaging modalities, micro-dissection and histological studies could help in better describing these paths.

It is possible to extract more 3D models from the µXCT data. However, because extraction and segmentation processes are time consuming, we focused on the auditory ossicles and osseous labyrinth. Previous reports mention 2 to 3 person-months to create a full 3D virtual model of the human temporal bone (Wang et al., 2006). Luckily, newer image processing algorithms could expedite this step (van den Boogert et al., 2018).

This study describes the anatomy of the middle and inner ear of the southern white rhino using µXCT imaging. Despite some unique particularities, it shows many similar traits to its well described human and equine counterparts. Further investigations are needed in order to provide a complete virtual model including both soft and bone tissues of this difficultly accessible region.

ACKNOWLEDGEMENTS

We wish to thank Dr. Michelle Otto, from Buffalo Dream Ranch, who provided us with the 2 baby rhinoceros heads. We acknowledge the DST-NRF for the financial support (Grant # UID72310) to establish the MIXRAD micro-focus X-ray tomography facility at Necsa.

CONFLICT OF INTEREST

The authors declare that this study was conducted in the absence of any commercial or financial relationships that could be seen as a potential conflict of interest.

ORCID

Mickaël P. Robert https://orcid.org/0000-0002-9497-3852

REFERENCES

Anonymous. (2018). *Rhino poaching statistics*. Retrieved from http://www.poachingfacts.com/poaching-statistics/rhino-poaching-statistics/

Baljit, S. (2017). *Dyce, Sack, and Wensing's textbook of veterinary anatomy*. : Saunders, An Imprint of Elsevier Limited, pp 872.

Barone, R. (2010). *Anatomie comparée des mammifères domestiques. Tome 7: Neurologie II*. : Vigot, pp 836.

Barone, R. (2011). *Anatomie comparée des mammifères domestiques. Tome 5: Angiologie*, 2nd edn. : Vigot, pp 904.

Botti, M., Secci, F., Ragionieri, L., Dessole, A. A., & Acone, F. (2006). Auditory ossicles in the ruminants: Comparative morphological analysis with the analogues formations of horse. *Annali della Facoltà di Medicina Veterinaria-Università di Parma (Italy)*, *26*, 91–96.

Buckingham, R. A., & Valvassori, G. E. (2001). Inner ear fluid volumes and the resolving power of magnetic resonance imaging: Can it differentiate endolymphatic structures? *The Annals of Otology, Rhinology, and Laryngology*, *110*(2), 113–117. https://doi.org/10.1177/000348940111000204

Collin, 2006Collin, B. (2006). *Anatomie du cheval*. : Derouaux Ordina Editions, pp 700.

Curtin, H., Gupta, R., & Bergeron, R. (2011). *Embryology, anatomy and imaging of the temporal bone. Head and Neck Imaging*, 5th edn. : Elsevier Mosby, 1058.

Doran, A. H. G. (1876). On the comparative anatomy of the auditory ossicles of the Mammalia. *Proceedings of the Royal Society of London*, *25*, 101–109.

Dudley, R. J., Wood, S. P., Hutchinson, J. R., & Weller, R. (2015). Radiographic protocol and normal anatomy of the hind feet in the white rhinoceros (*Ceratotherium simum*). *Veterinary Radiology & Ultrasound*, *56*(2), 124–132. https://doi.org/10.1111/vru.12215

Emslie, R. (2012). *Ceratotherium simum*. The IUCN Red List of Threatened Species 2012: e.T4185A16980466. Retrieved from https://doi.org/10.2305/IUCN.UK.2012.RLTS.T4185A16980466.en

Endo, H., Manglai, Fujisawa, M., Kurohmaru, M., & Hayashi, Y. (1998). The guttural pouch is not present in the white rhinoceros (*Ceratotherium simum*); morphology of the eustachian tube and nasopharynx. *Anatomia Histologia and Embryologia*, *27*(5), 327–330. https://doi.org/10.1111/j.1439-0264.1998.tb00202.x

Fritsch, G., Frey, R., Hermes, R., Goeritz, F., Strauss, G., Wibbett, G., & Hildebrandt, T. B. (2004). *Comparative study on rhinoceros head anatomy using endoscopy, computed tomography (CT) and gross anatomy*. Paper presented at the Proceedings of the AAZV, AAWV, WDA Joint Conference. 128–129.

Galateanu, G., Hildebrandt, T. B., Maillot, A., Etienne, P., Potier, R., Mulot, B., Saragusty, J., & Hermes, R. (2013). One small step for rhinos, one giant leap for wildlife management- imaging diagnosis of bone pathology in distal limb. *PLoS ONE*, *8*(7), e68493. https://doi.org/10.1371/journal.pone.0068493

Gerard, M. P., Glyphis, Z. G., Crawford, C., Blikslager, A. T., & Marais, J. (2018). Identification of a nasoconchal paranasal sinus in the white rhinoceros (*Ceratotherium simum*). *Journal of Zoo and Wildlife Medicine*, *49*(2), 444–449. https://doi.org/10.1638/2017-0185.1

Glueckert, R., Johnson Chacko, L., Schmidbauer, D., Potrusil, T., Pechriggl, E. J., Hoermann, R., Brenner, E., Reka, A., Schrott-Fischer, A., & Handschuh, S. (2018). Visualization of the membranous labyrinth and nerve fiber pathways in human and animal inner ears using MicroCT imaging. *Frontiers in Neuroscience*, *12*, 501. https://doi.org/10.3389/fnins.2018.00501

Green, J. D. Jr, Marion, M. S., Erickson, B. J., Robb, R. A., & Hinojosa, R. (1990). Three-dimensional reconstruction of the temporal bone. *Laryngoscope*, *100*(1), 1–4. https://doi.org/10.1288/00005537-199001000-00001

Hoffman, J., & de Beer, F. (2012). *Characteristics of the Micro-Focus x-Ray Tomography Facility (MIXRAD) at Necsa in South Africa*. Paper presented at the 18th World Conference on Nondestructive Testing, Durban, South Africa.

Hyrtl, J. (1873). *Die Corrosions-Anatomie und ihre Ergebnisse*. Braumüller.

Knight, M. (2017). African Rhino Specialist Group report. *Pachyderm*, *58*, 17–35.

Lee, D. H., Chan, S., Salisbury, C., Kim, N., Salisbury, K., Puria, S., & Blevins, N. H. (2010). Reconstruction and exploration of virtual middle-ear

models derived from micro-CT datasets. *Hearing Research*, *263*(1–2), 198–203. https://doi.org/10.1016/j.heares.2010.01.007

Lemonde.fr. (2018). Retrieved from http://www.Lemonde.fr/planete/article/2018/03/20/kenya-mort-de-sudan-le-dernier-rhinoceros-male-blanc-du-nord_5273465_3244.html

Mason, T. P., Applebaum, E. L., Rasmussen, M., Millman, A., Evenhouse, R., & Panko, W. (2000). Virtual temporal bone: Creation and application of a new computer-based teaching tool. *Otolaryngology – Head and Neck Surgery*, *122*(2), 168–173. https://doi.org/10.1016/S0194-5998(00)70234-8

Melhem, E. R., Shakir, H., Bakthavachalam, S., MacDonald, C. B., Gira, J., Caruthers, S. D., & Jara, H. (1998). Inner ear volumetric measurements using high-resolution 3D T2-weighted fast spin-echo MR imaging: Initial experience in healthy subjects. *AJNR. American Journal of Neuroradiology*, *19*(10), 1819–1822.

Moon, I. S., & Lee, W.-S. (2014). Internal carotid artery in the middle ear. *New England Journal of Medicine*, *371*(4), e5. https://doi.org/10.1056/NEJMicm1312261

Nayak, S. (2001). Segmental anatomy of the temporal bone. *Seminars in Ultrasound, CT and MRI*, *22*(3), 184–218. https://doi.org/10.1016/s0887-2171(01)90007-1

Owen, R. (1866). *On the anatomy of vertebrates - Volume III: Mammals*. : Longmans, Green and Co., pp 938.

Owen-Smith, R. N. (2013). Ceratotherium simum - white rhinoceros (grass rhinoceros, square-lipped rhinoceros). In J. Kingdon, & M. Hoffmann (Eds.), *Mammals of Africa – Vol. V* (pp. 446–454). Bloomsbury.

Qiu, M. G., Zhang, S. X., Liu, Z. J., Tan, L. W., Wang, Y. S., Deng, J. H., & Tang, Z. S. (2003). Plastination and computerized 3D reconstruction of the temporal bone. *Clinical Anatomy*, *16*(4), 300–303. https://doi.org/10.1002/ca.10076

Robin des Bois (2018). Notes on rhinoceros poaching. *On the Trail (Information and Analysis Bulletin on Animal Poaching and Smuggling)*, *19*, 83–91.

Schellhorn, R. (2018). A potential link between lateral semicircular canal orientation, head posture, and dietary habits in extant rhinos (Perissodactyla, Rhinocerotidae). *Journal of Morphology*, *279*(1), 50–61. https://doi.org/10.1002/jmor.20753

Sorensen, M. S., Dobrzeniecki, A. B., Larsen, P., Frisch, T., Sporring, J., & Darvann, T. A. (2002). The visible ear: A digital image library of the temporal bone. *ORL; Journal of Oto-Rhino-Laryngology and Its Related Specialties*, *64*(6), 378–381. https://doi.org/10.1159/000066089

TRAFFIC. (2018). *South Africa: Rhino poaching in 2017 almost matches 2016 figure, with KwaZulu Natal now bearing the brunt*. Retrieved from https://www.traffic.org/news/south-africa-rhino-poaching-in-2017-almost-matches-2016-figure-with-kwazulu-natal-now-bearing-the-brunt/

van den Boogert, T., van Hoof, M., Handschuh, S., Glueckert, R., Guinand, N., Guyot, J.-P., Kingma, H., Perez-Fornos, A., Seppen, B., Johnson Chacko, L., Schrott-Fischer, A., van de Berg, R., & (2018). Optimization of 3D-visualization of micro-anatomical structures of the human inner ear in osmium tetroxide contrast enhanced micro-CT scans. *Frontiers in Neuroanatomy*, *12*, 41. https://doi.org/10.3389/fnana.2018.00041

Vicq-D'Azyr, F., & Cloquet, H. (1819). *Encyclopédie Méthodique, Tome 3: Système Anatomique; Mammifères Et Oiseaux*. Veuve Agasse, pp 688.

Wang, H., Merchant, S. N., & Sorensen, M. S. (2007). A downloadable three-dimensional virtual model of the visible ear. *ORL; Journal of Oto-Rhino-Laryngology and Its Related Specialties*, *69*(2), 63–67. https://doi.org/10.1159/000097369

Wang, H., Northrop, C., Burgess, B., Liberman, M. C., & Merchant, S. N. (2006). Three-dimensional virtual model of the human temporal bone: A stand-alone, downloadable teaching tool. *Otology & Neurotology*, *27*(4), 452–457. https://doi.org/10.1097/01.mao.0000188353.97795.c5

Webster, D. B. (1966). Ear structure and function in modern mammals. *American Zoologist*, *6*(3), 451–466. https://doi.org/10.1093/icb/6.3.451

Wiet, G. J., Schmalbrock, P., Powell, K., & Stredney, D. (2005). Use of ultra-high-resolution data for temporal bone dissection simulation. *Otolaryngology – Head and Neck Surgery*, *133*(6), 911–915. https://doi.org/10.1016/j.otohns.2005.05.655

Wiet, G. J., Stredney, D., Sessanna, D., Bryan, J. A., Welling, D. B., & Schmalbrock, P. (2002). Virtual temporal bone dissection: An interactive surgical simulator. *Otolaryngology – Head and Neck Surgery*, *127*(1), 79–83. https://doi.org/10.1067/mhn.2002.126588

WitmerLab. (2012). *The visible interactive rhino*. Retrieved from https://people.ohio.edu/witmerl/3D_rhino.htm

SUPPORTING INFORMATION

Additional supporting information may be found online in the Supporting Information section.

How to cite this article: Robert MP, Carstens A, de Beer FC, Hoffman JW, Steenkamp G. Micro-anatomy of the ear of the southern white rhinoceros (*Ceratotherium simum simum*). *Anat Histol Embryol*. 2021;50:316–323. https://doi.org/10.1111/ahe.12632